Mesoscale modeling of vacancy-mediated Si segregation near an edge dislocation in Ni under irradiation

Zebo Li[1,2,*] and Dallas R. Trinkle[2,†]

[1]*Department of Materials Science and Engineering, University of Illinois at Urbana-Champaign, Urbana, Illinois 61801, USA*

[2]*Department of Nuclear, Plasma, and Radiological Engineering, University of Illinois at Urbana-Champaign, Urbana, Illinois 61801, USA*

(Received 16 December 2016; published 11 April 2017)

We use a continuum method informed by transport coefficients computed using self-consistent mean field theory to model vacancy-mediated diffusion of substitutional Si solutes in FCC Ni near an $\frac{a}{2}[1\bar{1}0](111)$ edge dislocation. We perform two sequential simulations: first under equilibrium boundary conditions and then under irradiation. The strain field around the dislocation induces heterogeneity and anisotropy in the defect transport properties and determines the steady-state vacancy and Si distributions. At equilibrium both vacancies and Si solutes diffuse to form Cottrell atmospheres with vacancies accumulating in the compressive region above the dislocation core while Si segregates to the tensile region below the core. Irradiation raises the bulk vacancy concentration, driving vacancies to flow into the dislocation core. The out-of-equilibrium vacancy fluxes drag Si atoms towards the core, causing segregation to the compressive region, despite Si being an oversized solute in Ni.

DOI: 10.1103/PhysRevB.95.144107

I. INTRODUCTION

Development of creep resistant methodologies has been gathering attentions for the past decades [1,2], especially for materials in nuclear reactors [3,4]. One practical and promising way to reduce or prevent creep is introducing appropriate solutes into materials [5–7] as precipitates, if formed, create obstacles against the motion of high-dimensional defects like dislocations [8]. Experimentally, the formation of precipitates under irradiation has been observed in alloys such as Si in Ni [9,10]. Designing alloys with improved creep resistance requires a predictive understanding of the transport of point defects (vacancies and self-interstitial atoms) and solutes near sinks under irradiation.

Irradiation and stress affect the diffusion of point defects and solute atoms in alloys. Irradiation creates collision cascades, producing a large number of Frenkel pairs and point defect clusters in the bulk [11,12]. This supersaturation of point defects induces out-of-equilibrium fluxes of vacancies and self-interstitials, which can drag solute atoms towards or away from sinks, depending on the kinetic correlations between solutes and point defects [13]. The stress fields generated by sinks such as dislocations or grain boundaries can also modify the diffusion properties of point defects and solutes [14]. Dederichs *et al.* [15] showed that stress can break the symmetry of the saddle-point configurations, causing anisotropy in the transport coefficients. Heterogeneous stress also modifies the driving forces, which are given by the gradients of chemical potentials [16,17].

Accurate modeling of defect diffusion requires a multiscale approach, with data from smaller length-scale models informing larger length-scale models. Modern density functional theory can provide energy barriers and vibrational frequencies required to compute transition rates for atomic jump events. Atomistic methods, like molecular dynamics and kinetic Monte Carlo simulations, can directly model atomic transport processes [18]. Purge *et al.* studied the self-diffusion in the cores of screw and edge dislocations in aluminum using molecular dynamics and showed that at high temperatures dislocation cores become effective sources or sinks for point defects and the effect of pre-existing defects on the dislocation mobility diminishes [19]. Sivak *et al.* used kinetic Monte Carlo to model diffusion of point defects in dislocation strain fields in body-centered cubic iron and vanadium and found that the dislocations are more efficient sinks for self-interstitial atoms than for vacancies [20]. However, atomistic simulations are typically limited to modeling systems with nanometer length scales over picosecond timescales, which prevents them from simulating diffusion in mesoscale systems over long times. The self-consistent mean field (SCMF) method [21,22] or a Green function approach [23] can compute the corresponding transport coefficients from the atomic jump rates to bridge the gap between microscopic atomic processes and macroscopic species transport. Phase field models [24,25] informed with precomputed transport coefficients can simulate diffusion processes with length scales up to millimeters over a timescale of days. Geslin *et al.* [26] and Ke *et al.* [27] used phase field methods to model dislocation climb based on vacancy diffusion. Both of these studies explicitly computed the climb rate as a function of external stress and showed the applicability of phase field methods to model creep, however they did not consider the effects of solutes. We use a related mesoscale method to model the coupled diffusion of vacancies and solute atoms, and focus on how the dislocation strain field and irradiation modify the configuration of the solute segregation.

We model vacancy-mediated diffusion of substitutional Si in face-centered cubic (FCC) Ni near an $\frac{a}{2}[1\bar{1}0](111)$ edge dislocation using precomputed transport coefficient data. Previous studies by Garnier *et al.* computed the atomic jump rates for Ni-Si alloys using density-functional theory [28] and obtained the corresponding transport coefficients as well as their strain derivatives using the SCMF method informed with strain-modified jump rates [14,29]. In our model we only consider the diffusion of vacancies and Si solutes because self-interstitial atoms formed under irradiation diffuse quickly and

*zeboli1@illinois.edu

†dtrinkle@illinois.edu

are annihilated at sinks like dislocations or grain boundaries on a short timescale, leaving behind a highly saturated vacancy environment in the bulk crystal [30]. Furthermore, the self-interstitials interact weakly with oversized substitutional solutes like Si in Ni, compared with vacancies [31,32]. In this paper, we first describe the details of our mesoscale model in Sec. II along with the simulation choices in Sec. III. We perform two sequential simulations: first at equilibrium and second under irradiation. Section IV presents and discusses the simulation results. Finally, Sec. V provides conclusions and discusses extensions of the methodology.

II. MESOSCALE MODEL

In the framework of thermodynamics of irreversible processes [17], driving forces and transport coefficients determine the fluxes of species in a multicomponent system. Transport coefficients linearly relate fluxes of each species to driving forces. For vacancy-mediated diffusion of Si in the dilute limit, gradients of chemical potentials for vacancies μ_{V} and silicon μ_{Si} produce fluxes $\mathbf{J}_{\mathrm{V}}$ and $\mathbf{J}_{\mathrm{Si}}$ in both species [14,17],

$$\begin{aligned}\mathbf{J}_{\mathrm{V}} &= -\underline{L}_{\mathrm{VV}}\nabla\mu_{\mathrm{V}} - \underline{L}_{\mathrm{VSi}}\nabla\mu_{\mathrm{Si}},\\ \mathbf{J}_{\mathrm{Si}} &= -\underline{L}_{\mathrm{SiV}}\nabla\mu_{\mathrm{V}} - \underline{L}_{\mathrm{SiSi}}\nabla\mu_{\mathrm{Si}}.\end{aligned} \tag{1}$$

The transport coefficients are strain-dependent second-rank tensors: $\underline{L}_{\mathrm{VV}}$, $\underline{L}_{\mathrm{SiV}} = \underline{L}_{\mathrm{VSi}}$, and $\underline{L}_{\mathrm{SiSi}}$. The off-diagonal term $\underline{L}_{\mathrm{SiV}}$ is crucial to solute transport under irradiation, when the Si atoms are dragged by the out-of-equilibrium vacancy fluxes created by irradiation. Consequently, Si can segregate at vacancy sinks such as dislocations, where vacancies are annihilated but solute atoms are not.

The chemical potentials μ_{V} and μ_{Si} that provide driving forces for the diffusion depend on the volumetric strain and also capture the interactions between species. For dilute vacancy and Si concentrations in the small strain limit [17],

$$\begin{aligned}\mu_{\mathrm{V}} &= \alpha_{\mathrm{V}}\epsilon_{\mathrm{v}} + k_{\mathrm{B}}T\ln\left(\gamma_{\mathrm{V}}c_{\mathrm{V}}/c_{\mathrm{V}}^0\right),\\ \mu_{\mathrm{Si}} &= \alpha_{\mathrm{Si}}\epsilon_{\mathrm{v}} + k_{\mathrm{B}}T\ln\left(\gamma_{\mathrm{Si}}c_{\mathrm{Si}}/c_{\mathrm{Si}}^0\right),\end{aligned} \tag{2}$$

where k_{B} is the Boltzmann constant, T is the temperature, γ is the activity, c is the atomic fraction, and c^0 the equilibrium concentration. Both the vacancy and Si have isotropic elastic dipoles (derivative of energy with respect to strain), so the chemical potentials μ_{V} and μ_{Si} vary linearly with volumetric strain ϵ_{v} with coefficients $\alpha_{\mathrm{V}} = 6.37$ eV and $\alpha_{\mathrm{Si}} = -0.251$ eV [28]. The Si equilibrium concentration corresponds to the specific alloy, while $c_{\mathrm{V}}^0 = \exp(-E_f/k_{\mathrm{B}}T)$ for vacancy formation energy $E_v^{\mathrm{f}} = 1.63$ eV [28]. The activity coefficients γ_{V} and γ_{Si} capture solute-vacancy interaction effects on chemical potentials. We use a low-temperature expansion for dilute concentrations [33,34] for γ_{V} and γ_{Si},

$$\begin{aligned}\gamma_{\mathrm{V}} &= 1 + c_{\mathrm{Si}}\sum_j Z_j(e^{-\Delta g_j/k_{\mathrm{B}}T} - 1),\\ \gamma_{\mathrm{Si}} &= 1 + c_{\mathrm{V}}\sum_j Z_j(e^{-\Delta g_j/k_{\mathrm{B}}T} - 1),\end{aligned} \tag{3}$$

TABLE I. Transport coefficients [1/(eV Å ns)] and their derivatives with strains at $T = 960$ K from Ref. [14]. In the dilute limit, $\underline{L}_{\mathrm{VV}}$ is proportional to c_{V} while $\underline{L}_{\mathrm{SiV}}$ and $\underline{L}_{\mathrm{SiSi}}$ are proportional to $c_{\mathrm{V}}c_{\mathrm{Si}}$.

AB	L_{AB}^0	L_{AB}^{v}	L_{AB}^{t}
VV	$1.52\times10^{-1}c_{\mathrm{V}}$	$1.29\times10^{1}c_{\mathrm{V}}$	$-7.42\times10^{0}c_{\mathrm{V}}$
SiV	$1.57\times10^{-1}c_{\mathrm{V}}c_{\mathrm{Si}}$	$1.33\times10^{1}c_{\mathrm{V}}c_{\mathrm{Si}}$	$-2.24\times10^{1}c_{\mathrm{V}}c_{\mathrm{Si}}$
SiSi	$1.29\times10^{0}c_{\mathrm{V}}c_{\mathrm{Si}}$	$1.09\times10^{2}c_{\mathrm{V}}c_{\mathrm{Si}}$	$-5.08\times10^{1}c_{\mathrm{V}}c_{\mathrm{Si}}$

with Z_j sites in shell j with binding energy Δg_j. Silicon and nickel vacancies have interactions out to the third shell. Garnier *et al.* [28] found an attractive $\Delta g_1 = -0.0996$ eV ($Z_1 = 12$), a small $\Delta g_2 = 0.0120$ eV ($Z_2 = 6$), and a repulsive $\Delta g_3 = 0.0452$ eV ($Z_3 = 24$).

The strain field created by an edge dislocation induces heterogeneity and anisotropy in defect transport coefficients. The strain tensor $\underline{\epsilon}$ can be decomposed into volumetric strain $\underline{\epsilon}_{\mathrm{v}} = \frac{1}{3}\epsilon_{\mathrm{v}}\underline{1}$ (where $\underline{1}$ is the identity matrix), tetragonal strain $\underline{\epsilon}_{\mathrm{t}}$ along cube axes $\langle100\rangle$, and shear strain $\underline{\epsilon}_{\mathrm{s}}$,

$$\underline{\epsilon} = \tfrac{1}{3}\epsilon_{\mathrm{v}}\underline{1} + \underline{\epsilon}_{\mathrm{t}} + \underline{\epsilon}_{\mathrm{s}}. \tag{4}$$

For a system with cubic symmetry, the transport coefficient tensor $\underline{L}_{AB}(\underline{\epsilon})$ can be expanded as [14]

$$\underline{L}_{AB} = L_{AB}^0\underline{1} + L_{AB}^{\mathrm{v}}\tfrac{1}{3}\epsilon_{\mathrm{v}}\underline{1} + L_{AB}^{\mathrm{t}}\underline{\epsilon}_{\mathrm{t}} + L_{AB}^{\mathrm{s}}\underline{\epsilon}_{\mathrm{s}}, \tag{5}$$

where L_{AB}^0 is the stress-free value, and L_{AB}^{v}, L_{AB}^{t}, and L_{AB}^{s} are the strain derivatives [15]. For the Ni-Si system, the shear strain contribution to the atomic jump frequencies is negligible so $L_{AB}^{\mathrm{s}} \approx 0$ [28]. For an $\frac{a}{2}[1\bar{1}0](111)$ edge dislocation in FCC Ni, a natural coordinate system (the dislocation frame) is formed by the Burgers vector $\mathbf{b} = \frac{a}{2}[1\bar{1}0]$ (a is the lattice parameter for FCC Ni), the slip plane normal $\mathbf{n} = [111]$, and the threading vector $\mathbf{t} = [\bar{1}\bar{1}2]$. Garnier *et al.* computed transport coefficients of the Ni-Si-vacancy system for $T = 960$ K, 1060 K, and 1160 K, which show positive, zero, and negative off-diagonal transport coefficients L_{SiV}^0 [14]. The $\underline{L}_{AB}$ tensor component in the $\mathbf{b}\times\mathbf{n}$ plane is [14]

$$\underline{L}_{AB} = \begin{pmatrix} L_{AB}^0 + \frac{1}{3}L_{AB}^{\mathrm{v}}\epsilon_{\mathrm{v}} + \frac{1}{6}L_{AB}^{\mathrm{t}}\epsilon_{bb} & \frac{2}{3}L_{AB}^{\mathrm{t}}\epsilon_{bn} \\ \frac{2}{3}L_{AB}^{\mathrm{t}}\epsilon_{bn} & L_{AB}^0 + \frac{1}{3}L_{AB}^{\mathrm{v}}\epsilon_{\mathrm{v}} \end{pmatrix}, \tag{6}$$

and the values of L_{AB}^0, L_{AB}^{v}, and L_{AB}^{t} are listed in Table I for $T = 960$ K. Indeed, for the special case of Ni-Si alloy, Garnier *et al.* [28] have shown an interesting result that the derivatives of migration barriers with respect to volumetric strain $\partial E_{\mathrm{m}}/\partial\epsilon_{\mathrm{v}}$ is a constant for all types of atomic jumps in the system. Since the migration barriers have good linear dependences on the volumetric strain ϵ_{v} in a larger strain range than that for L_{AB} [28,29], we use the following expression instead of Eq. (6) to

denote $\underline{L}_{AB}$ to achieve a better accuracy,

$$\underline{L}_{AB} = \begin{pmatrix} L^0_{AB} \cdot \exp\left(-\frac{\partial E_m/\partial \epsilon_v}{k_B T}\epsilon_v\right) + \frac{1}{6}L^t_{AB}\epsilon_{bb} & \frac{2}{3}L^t_{AB}\epsilon_{bn} \\ \frac{2}{3}L^t_{AB}\epsilon_{bn} & L^0_{AB} \cdot \exp\left(-\frac{\partial E_m/\partial \epsilon_v}{k_B T}\epsilon_v\right) \end{pmatrix}, \tag{7}$$

where the migration barrier derivatives $\partial E_m/\partial \epsilon_v \equiv -2.336$ eV, which is proportional to the ratio between L^v_{AB} and L^0_{AB}.

We choose a simulation temperature $T = 960$ K, for which $L^0_{SiV} > 0$ and a positive solute-vacancy drag is expected. In the dilute limit, $\underline{L}_{VV}$ is proportional to c_V while $\underline{L}_{SiV}$ and $\underline{L}_{SiSi}$ are proportional to $c_V c_{Si}$. We use isotropic elasticity theory for the edge dislocation strain field in the plane of the dislocation line: $\epsilon_v = -b\sin\theta/4\pi r$, $\epsilon_{bn} = b(\cos\theta\cos 3\theta)/16\pi r$, and $\epsilon_{bb} = -b(4+3\cos 2\theta)\sin\theta/8\pi r$, where r is the distance from the dislocation, and θ is the angle from the slip plane. Therefore near an edge dislocation, both transport coefficients and chemical potentials are spatially dependent, and transport coefficients are anisotropic due to nonzero ϵ_{bn} and ϵ_{bb}. All three strain components become singular at $r = 0$ and decay as r^{-1}.

III. SIMULATION SETUP

The simulation domain is an annular region with inner radius r_{in} and outer radius r_{out} in the $\mathbf{b} \times \mathbf{n}$ plane. Since an edge dislocation has translational symmetry along the threading vector $\mathbf{t}$, for simplicity we project the 3D diffusion system into a 2D plane perpendicular to $\mathbf{t}$, i.e. the $\mathbf{b} \times \mathbf{n}$ plane. We use a polar coordinate system centered at the dislocation, which is natural for simulating an edge dislocation due to the separability of the strain in r and θ. The mesoscale equations are singular at $r = 0$ in the elastic strain components ϵ_v, ϵ_{bb}, and ϵ_{bn}. We choose an inner radius $r_{in} = 2a$ to exclude the dislocation core from the simulation region, ensuring that all three strain components are below 3% to validate the small strain approximation used in Eq. (2) and Eq. (7). We use an outer boundary condition to capture the vacancy saturation due to irradiation instead of allowing vacancies to be produced or recombined throughout the simulation region. The outer radius is chosen as $r_{out} = 14.5a$ (50 Å), which we find is small enough to ignore the production and annihilation of vacancies within the simulation region while large enough to model the irradiation-induced solute segregation for our simulations. However, the model employed in this work is also suitable for larger length scale systems up to microns or even millimeters. The variation in the strain fields and point defect distribution requires a denser distribution of small radial points with equal spacing of angular points; we use a uniform mesh in the angular direction and a logarithmic mesh in the radial direction. For an $N_\theta \times N_r$ mesh, the grid point (r_i, θ_j) is located at $r_i = r_{in}\exp(\frac{i}{N_r}\ln(r_{out}/r_{in}))$ for $i = 0,1,\ldots,N_r$ and $\theta_j = \frac{j}{N_\theta}2\pi$ for $j = 0,1,\ldots,N_\theta$, with periodic boundary conditions for θ. We use a 100×100 mesh for the present simulations.

We apply appropriate boundary conditions at the inner boundary $r = r_{in}$ to simulate the dislocation core interaction with vacancies and solutes. We treat the core as a perfect sink for vacancies by assuming that vacancies diffuse fast enough near the sink to maintain the spatially dependent equilibrium vacancy concentration $c^{EQ}_V(\mathbf{r})$ in the core and at the core boundary. The equilibrium solution for the vacancy concentration due to the dislocation strain field is determined by setting $\mu_V = 0$ in Eq. (2),

$$c^{EQ}_V(r,\theta) = \frac{c^0_V}{\gamma_V}\exp\left(-\frac{\alpha_V \epsilon_v(r,\theta)}{k_B T}\right), \tag{8}$$

which depends on the local volumetric strain $\epsilon_v(r,\theta)$. We fix the vacancy concentration c_V at the inner boundary to be the equilibrium vacancy concentration,

$$c_V(r_{in},\theta) = c^{EQ}_V(r_{in},\theta). \tag{9}$$

The vacancy activity γ_V depends on the local Si concentration c_{Si} so it must be computed adaptively during the simulations. Since Si atoms cannot be absorbed or created by the dislocation core, we fix the normal flux of Si at the inner boundary to be zero,

$$\hat{\mathbf{r}} \cdot \mathbf{J}_{Si}|_{r=r_{in}} = 0, \tag{10}$$

where $\hat{\mathbf{r}}$ is the unit vector along the radial direction.

We perform sequential simulations of vacancy-mediated diffusion of substitutional Si in FCC Ni near an edge dislocation: first under equilibrium boundary conditions, which provides initial conditions for the second simulation of diffusion under irradiation. We apply the equilibrium vacancy concentration as the outer boundary condition for c_V,

$$c_V(r_{out},\theta) = c^{EQ}_V(r_{out},\theta). \tag{11}$$

The bulk Si concentration is 0.5% ensuring that Si is in the dilute limit,

$$c_{Si}(r_{out},\theta) = 5 \times 10^{-3} \tag{12}$$

as the outer boundary condition for c_{Si}. For the first simulation, vacancies and Si solutes are initially uniformly distributed and evolve towards their equilibrium distributions in the presence of the dislocation strain field. After the system reaches equilibrium, we study how irradiation modifies the diffusion behavior of vacancies and Si solutes. As irradiation creates an oversaturation of vacancies in the bulk, we change the outer boundary condition for vacancies to be

$$c_V(r_{out},\theta) = 10^{-7}, \tag{13}$$

which is approximately one and a half orders of magnitude larger than the equilibrium concentration. The saturated bulk vacancy concentration can be several orders of magnitude larger than the equilibrium value, depending on the irradiation rate [35–37]. The outer boundary condition for Si is the same as in the equilibrium case. We run both simulations for two days of simulation time, which is sufficient for both vacancies and Si to reach their steady state.

To capture the large timescale difference between vacancy diffusion and Si diffusion, we apply adaptive time steps in

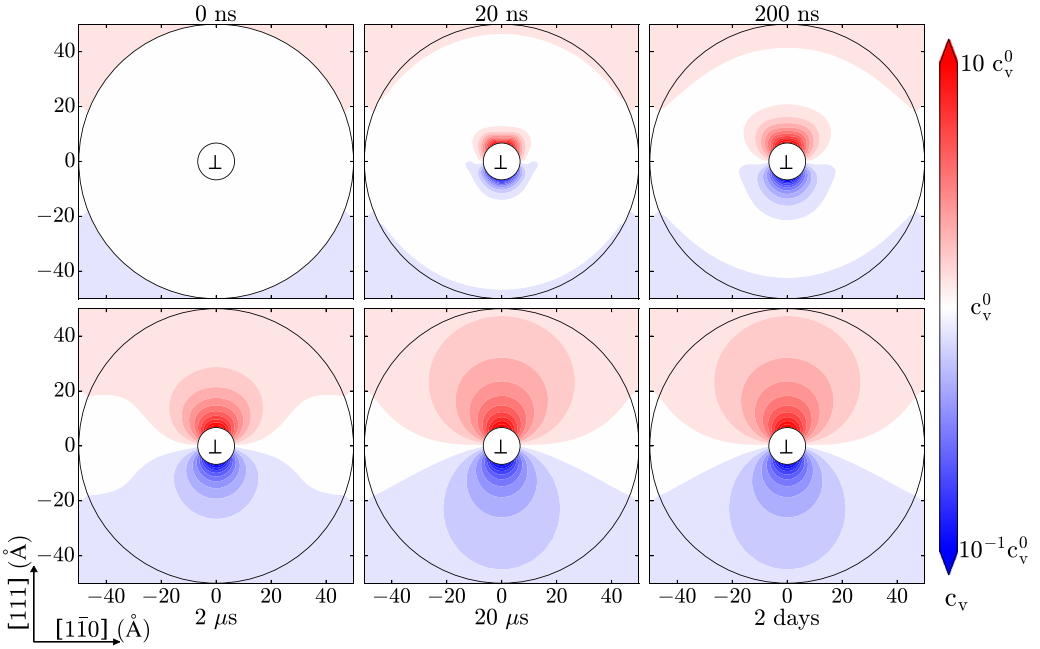

FIG. 1. Time evolution of the vacancy distribution around an edge dislocation under equilibrium boundary conditions. Initially vacancies are uniformly distributed with concentration $c_V = c_V^0 = 2.77 \times 10^{-9}$. The vacancy distribution evolves due to the presence of the dislocation strain field until it reaches a steady state configuration after 20 μs. At steady state, vacancies accumulate in the energetically favorable compressive region and are depleted from the energetically unfavorable tensile region, forming a Cottrell atmosphere. We evolve the diffusion systems for two days of simulation time, which allows both vacancies and Si to reach their steady-state configurations. (Contour plots for vacancy concentrations use log scale relative to c_V^0 to capture the large spacial variation near the dislocation core without losing features in the far-field area. Vacancy concentration outside the simulation region is set at equilibrium value to help illustrate the outer boundary condition for vacancies.)

the simulation. Our simulations show that vacancies diffuse quickly and reach their steady state in microseconds, while Si atoms diffuse much slower and reach their steady state over hours. A fixed time step has difficulty with diffusion processes over vastly different timescales, so we use an adaptive time-step scheme in which the time step Δt is determined by:

$$\Delta t = 10^{-1} \cdot \min\left\{\frac{c_V}{|\dot{c}_V|}, \frac{c_{Si}}{|\dot{c}_{Si}|}\right\}, \tag{14}$$

where $\dot{c}_V$ and $\dot{c}_{Si}$ are the time derivatives of the vacancy and Si concentrations and the minimum is computed over the entire simulation domain. Equation (14) ensures that during each step, the relative changes in the species concentrations do not exceed 10%, which leads to numerically stable simulations while the time step Δt increases with time. Initially, the vacancy concentration changes determines Δt, and after vacancies reach their steady state, the time step Δt is dominated by the slowly changing Si concentration. All of the simulation has been implemented using FiPy [38], a finite volume partial differential equation solver, developed mainly for phase-field simulations.

IV. SIMULATION RESULTS

Figure 1 shows that under equilibrium boundary conditions vacancies diffuse to form a Cottrell atmosphere at steady state. Even though both species have an initial uniform distribution, the heterogeneous volumetric strain field created by the dislocation induces spatial variation in the chemical potentials, driving vacancies and solutes to diffuse. For vacancies, since $\alpha_V > 0$, the chemical potential gradient drives the vacancies from the tensile region towards the compressive region, where they accumulate. At steady state, when the vacancy concentration profile stops evolving with time, a Cottrell atmosphere is formed around the dislocation with vacancy segregation above the core and depletion of vacancies below the core.

Figure 2 shows that around an edge dislocation the Si concentration profile also evolves towards a Cottrell atmosphere but with segregation in the tensile region and depletion in the compressive region and that the evolution process takes longer than for vacancies. Similar to the vacancy case, the strain dependent term in the chemical potential $\alpha_{Si}\epsilon_v$ influences the steady-state Si distribution at equilibrium. However, since Si is an oversized solute in Ni $\alpha_{Si} < 0$, the tensile region is energetically favored and therefore, the Si atoms segregate in the tensile region and are depleted from the compressive region. The Si concentration profile reaches its steady state after 10 hours, which is nine orders of magnitudes slower than the vacancy evolution. In the dilute limit, the diffusivity $\underline{D}_A$ for a species A, is related to the corresponding transport coefficient $\underline{L}_{AA}$,

$$\underline{D}_A = \lim_{c_A \to 0} \frac{\Omega k_B T}{c_A} \underline{L}_{AA}, \tag{15}$$

for atomic volume Ω and concentration c_A; thus, the Si diffusivity is proportional to the vacancy concentration while the vacancy diffusivity is not. After vacancies reach their

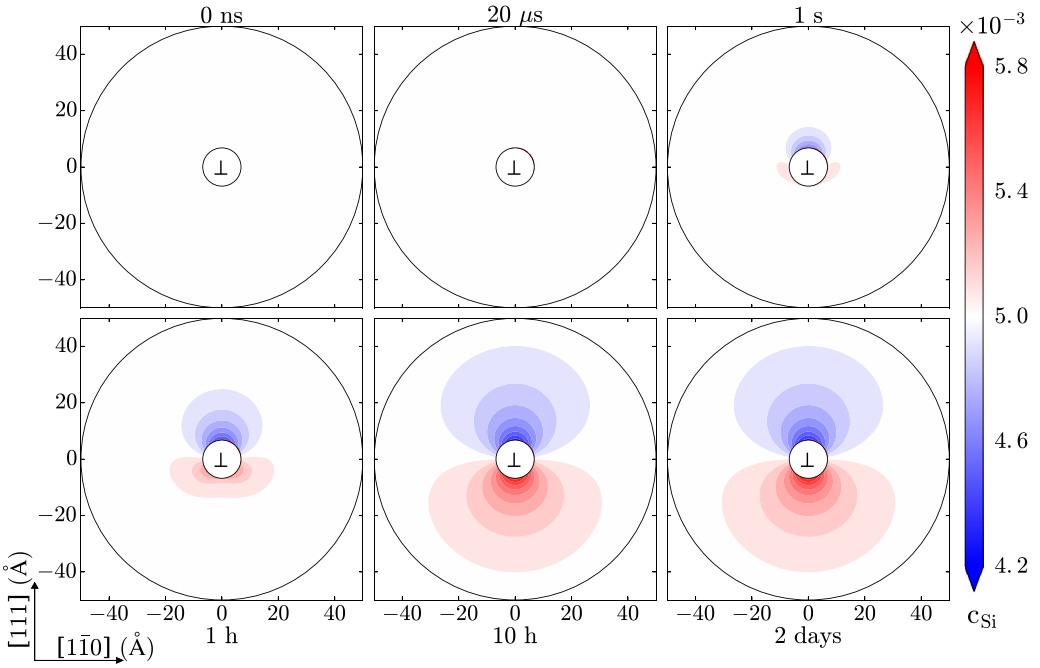

FIG. 2. Time evolution of the Si distribution around an edge dislocation under equilibrium boundary conditions. The Si profile also starts from a uniform distribution with Si concentration $c_{\mathrm{Si}} = c^0_{\mathrm{Si}} = 0.5\%$ and evolves due to dislocation strain fields. The Si atoms diffuse much slower than vacancies and reach the steady-state configuration after 10 hours. Similar to the vacancy case, the Si atoms form a Cottrell atmosphere at steady state segregating to the tensile region and are depleted from the compressive region.

steady-state configuration, the depleted vacancy concentration below the core slows the transport of Si atoms; this creates the intermediate state where Si atoms are concentrated in two lobe-shaped regions just below the slip plane on the edge of the vacancy depletion region. The Si atoms in these lobe-shaped regions continue to diffuse slowly into the vacancy depletion region and by $t = 10$ h have segregated below the core.

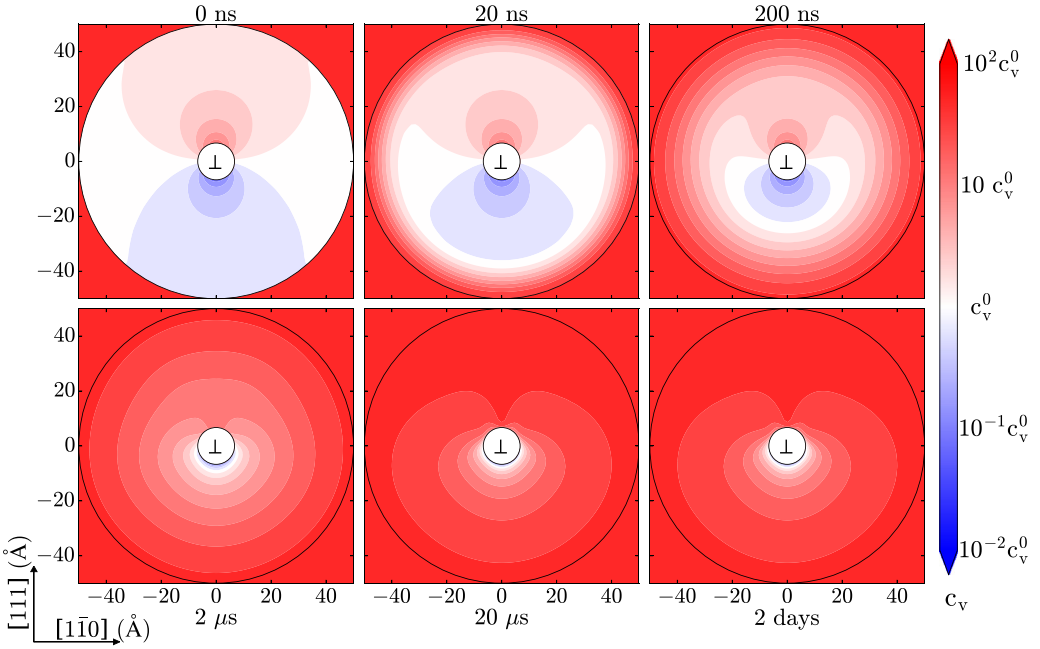

FIG. 3. Time evolution of the vacancy distribution near an edge dislocation under irradiation. At $t = 0$ ns, both species are at equilibrium and they evolve due to the presence of irradiation. Irradiation produces a highly saturated vacancy environment in the far-field region, causing a large number of vacancies to flow into the simulation region. At steady state, the tensile region is no longer depleted of vacancies and there is a large vacancy concentration gradient in the radial direction pointing from the outer boundary near the bottom of the simulation region to the inner core; c.f., Fig. 5.

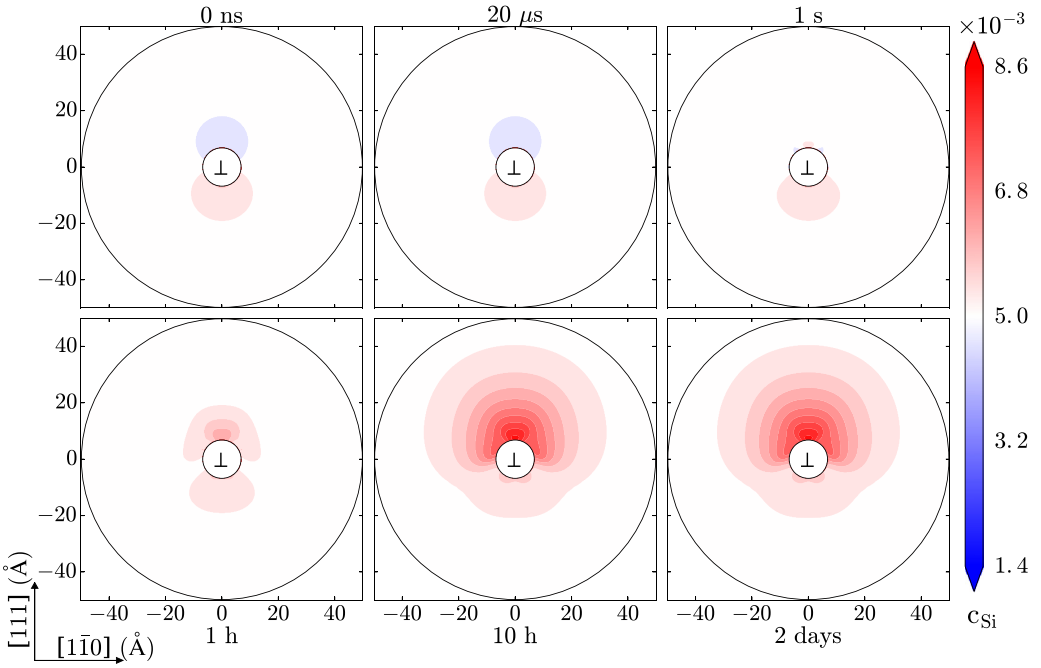

FIG. 4. Time evolution of solute (Si) concentration profile under irradiation, starting from the equilibrium Si distribution. Under irradiation, vacancy drag on Si atoms dominates the Si flux field causing Si to move toward the compressive region above the core. At steady state, more Si atoms segregate above the core than below the core, with the maximum Si concentration approaching twice the far field Si concentration $c^0_{\mathrm{Si}} = 0.5\%$.

Figure 3 shows as irradiation raises the vacancy concentration in the outer boundary, vacancies flow towards the dislocation core. At $t = 0$ ns, irradiation produces a highly saturated vacancy environment in bulk, while vacancies within the simulation region are still at the equilibrium distribution. Vacancies flow from the outer boundary towards the dislocation core. At 20 μs vacancies reach their steady-state configuration, where the depletion region below the core has disappeared and the entire simulation region is oversaturated with vacancies. At steady state, the vacancy driving force $\nabla\mu_{\mathrm{V}}$ does not vanish and vacancies continue to flow to the core, though $\dot{c}_{\mathrm{V}}$. This is shown in Fig. 4 which shows that at 20 μs, there are nonzero vacancy fluxes towards the core from all directions even though vacancies have reached their steady-state distribution.

Figure 4 shows that irradiation generates an unexpected enrichment of Si in the compressive region above the core, despite the fact that Si is oversized in FCC Ni. Since both the inner and outer boundary conditions for Si are the same as in the equilibrium case, the evolution of Si distribution under irradiation is completely due to the out-of-equilibrium vacancy fluxes. The positive off-diagonal transport coefficient $\underline{L}_{\mathrm{SiV}}$ linearly relates the Si flux $\mathbf{J}_{\mathrm{Si}}$ to the vacancy driving force $\nabla\mu_{\mathrm{V}}$, which drags Si solutes towards the inner core. Since Si atoms cannot be absorbed by the core, they accumulate around the core, creating a solute chemical potential gradient $\nabla\mu_{\mathrm{Si}}$ that drives Si away from the core. At steady state, both driving forces must be balanced so that there is no Si flux along the radial direction. The vacancy fluxes $\mathbf{J}_{\mathrm{V}}$ are larger in the compressive region (as Fig. 4 shows) and thus drag more Si atoms to segregate above the core.

Figures 5(a) and 5(b) show that at the beginning of the simulation under equilibrium conditions, the heterogeneous strain fields around an edge dislocation induce complex flow patterns for homogeneously distributed vacancies and Si solutes. The vacancies and Si are uniformly distributed initially. When the dislocation is introduced, the initial fluxes of both species show heterogeneity due to spatial variation of the chemical potential created by nonuniform volumetric strain $\epsilon_{\mathrm{v}}(\mathbf{r})$, as well as anisotropy due to the effect of nonzero ϵ_{bb} and ϵ_{bn} on the transport coefficients. Vacancies flow from the tensile region below the core to the compressive region above the core, which leads to the steady-state Cottrell atmosphere vacancy distribution shown in the last subfigure of Fig. 1. The Si solutes move in the opposite direction, which explains that Si atoms segregate to the tensile region and are depleted from the compressive region.

Figures 5(c) and 5(d) show that at 20 μs of irradiation a vacancy flux field flows into the inner boundary, which drags Si solutes towards the dislocation core. Under irradiation, vacancies reach the steady-state configuration at 20 μs while Si still appears to be at the equilibrium distribution. Irradiation modifies the flow patterns of both vacancies and Si. The difference between the highly saturated vacancy concentration in the far-field region and the equilibrium vacancy concentration at the inner core leads to the steady-state vacancy flux field directed toward the core. The vacancy fluxes have larger magnitudes in the compressive region above the core and relatively smaller magnitudes in the tensile region below the core. The directions and relative magnitudes of the Si fluxes are similar to that of the vacancies, suggesting that the flow of Si atoms is dominated by the positive vacancy drag $\underline{L}_{\mathrm{SiV}}\nabla\mu_{\mathrm{V}}$ ($L^0_{\mathrm{SiV}} > 0$). The Si atoms are dragged by vacancies towards

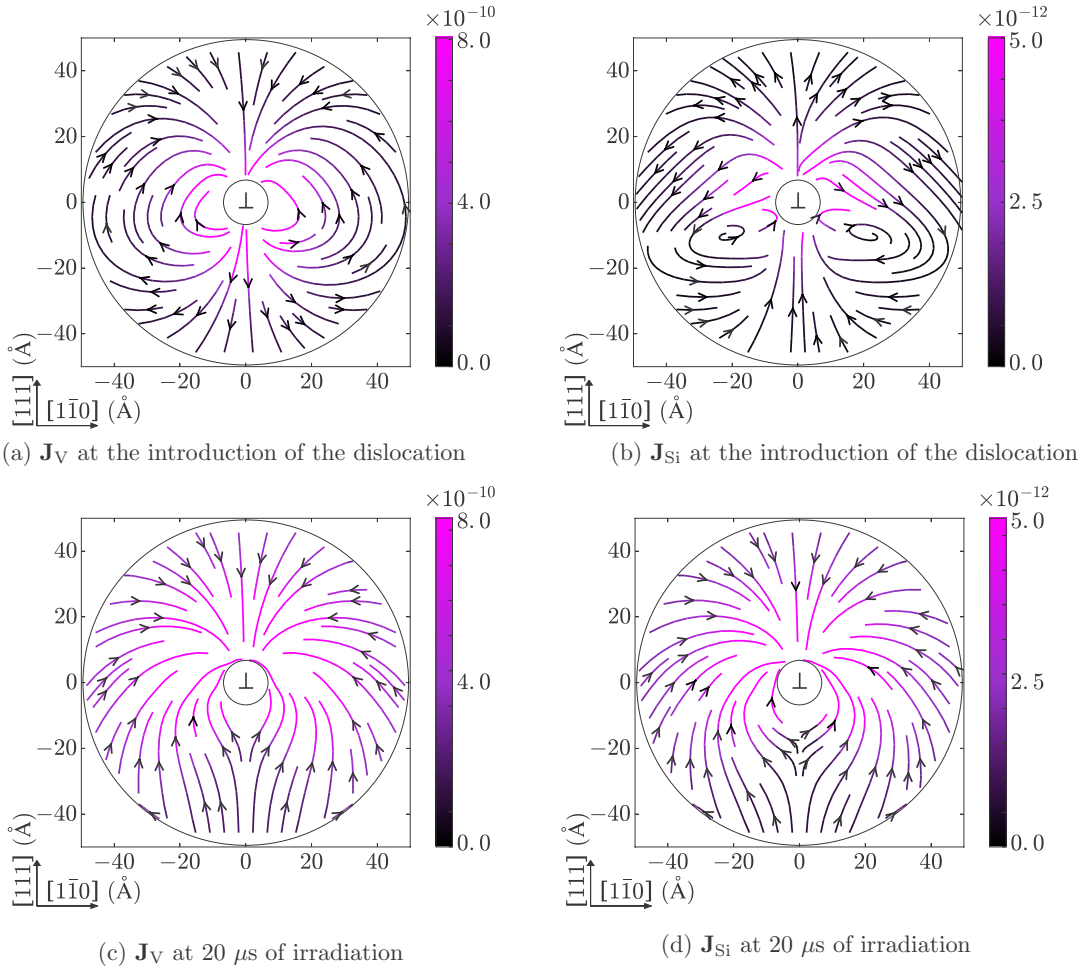

(a) $\mathbf{J}_{\mathrm{V}}$ at the introduction of the dislocation

(b) $\mathbf{J}_{\mathrm{Si}}$ at the introduction of the dislocation

(c) $\mathbf{J}_{\mathrm{V}}$ at 20 μs of irradiation

(d) $\mathbf{J}_{\mathrm{Si}}$ at 20 μs of irradiation

FIG. 5. Flow streams around an edge dislocation for (a) vacancies at the introduction of the dislocation, (b) Si at the introduction of the dislocation, (c) vacancies at 20 μs after irradiation, and (d) Si at 20 μs after irradiation. Color coding indicates the magnitude of fluxes with units: [1/(Å^2 ns)]. At the beginning of the equilibrium simulation when both species are uniformly distributed, vacancies flow from the tensile region below the core to the compressive region above the core, while Si atoms move in the opposite way. The anisotropy of both fluxes comes from the anisotropy of transport coefficients and the heterogeneity of volumetric strain which influences the chemical potentials. At 20 μs of irradiation, vacancies reach the steady-state configuration while Si stays at the equilibrium distribution. Irradiation creates a vacancy flux field flowing into the core from all directions, with larger flux magnitudes in the compressive region than in the tensile region. The Si fluxes show similar flow pattern to that of the vacancy.

the sink and accumulate around the dislocation core, which explains the out-of-equilibrium Si segregation. More Si atoms segregate to the compressive region where the vacancy fluxes have larger magnitudes than to the tensile region, despite the fact that they are oversized in Ni.

V. CONCLUSIONS

We use a mesoscale model to simulate vacancy-mediated diffusion of substitutional Si solutes in FCC Ni near a [1$\bar{1}$0](111) edge dislocation: first under equilibrium conditions and then under irradiation. The dislocation strain field and irradiation play crucial roles in determining point defect and solute diffusion behavior. Near the edge dislocation, the spatial variation of volumetric strain ϵ_{v} causes heterogeneity in the defect transport coefficients and chemical potentials, with the transport coefficients also being anisotropic due to nonzero ϵ_{bb} and ϵ_{bn}. These effects create complex vacancy and Si fluxes even though both species are uniformly distributed at the beginning of the simulation and determine the equilibrium distributions. In the presence of the dislocation strain field, both vacancies and Si solutes diffuse to form a Cottrell atmosphere with vacancies segregating to the compressive region above the core and Si segregating to the tensile region below the core. Irradiation raises the bulk vacancy concentration, driving vacancies to flow into the dislocation core, where the equilibrium vacancy concentration is imposed (perfect sink assumption). Although irradiation does not directly modify the solute distribution, the out-of-equilibrium steady-state vacancy flux drags Si atoms towards the dislocation core due to the positive coupling between Si and vacancies at the simulation temperature $T = 960$ K. This results in segregation in the compressive region, despite the fact that Si is an oversized solute in Ni.

Several approximations have been used in the current study. First of all, we assume both species are in the dilute limit, at

which only vacancy-solute pairs are considered in the cluster expansion and the SCMF solution is accurate [14,22]. In our system, the vacancy concentration c_V is below 10^{-7} and the Si concentration c_{Si} is around 0.5%, in which scenario we can estimate the contribution from three or more-body vacancy-Si clusters is roughly 1% of that from vacancy-Si pairs. Second, we use a small strain limit to validate the linearities in Eq. (2) and Eq. (7). In our simulation region, the inner radius is picked so that the volumetric strain is below 3% and the tetragonal component along cube axes ⟨100⟩ is below 1%, which guarantees that the migration barrier E_m and transport coefficients $\underline{L}_{AB}$ have good linear dependences on strains [28,29]. Last, we apply inner boundary conditions for both species rather than simulating the dislocation core region ($r < r_{in}$). This choice is partly motivated by the inaccuracy of using the current mesoscale method to model the highly distorted core region. On the other hand, we believe that these boundary conditions are reasonable approximations. The equilibrium boundary condition for vacancies is equivalent to treating the dislocation as a perfect sink, which has been used in prior works [26,27] and proven to be valid. The zero normal-flux boundary condition is to maintain the conservation law of Si atoms, considering the fact that Si atoms cannot be created or be annihilated at an isolated dislocation. This model ignores the effects from pipe diffusion and dislocation motion. To cover all these effects, an improvement can be done by developing an atomistic model, increasing accuracy with a decrease in efficiency, to explicitly simulate the dislocation core, and coupled with the present mesoscale simulation at the core boundary.

In this study we have focused on a specific diffusion process that leads to irradiation-driven Si segregation around an edge dislocation in Ni, but the multiscale methodology has other applications. The Onsager transport equations [Eq. (1)] as well as the expressions for species chemical potentials [Eq. (2)] and transport coefficients [Eq. (5)] can be applied to describe diffusion in other defect systems such as free surfaces or grain boundaries. Moreover, the continuum model can be extended to model systems with larger length scales up to millimeters, and simulate more complex diffusion processes, such as solutes segregating to extended defects including dislocation loops, grain boundaries, and interfaces.

ACKNOWLEDGMENT

This research is supported by the U.S. Department of Energy (DOE), Office of Science, Basic Energy Sciences (BES) under Award DE-FG02-05ER46217.

[1] G. Merckling, Specifications for creep-resistant steels: Europe, in *Creep-Resistant Steels* (Woodhead Publishing, Sawston, Cambridge, England, 2008), pp. 78–154.
[2] F. Masuyama, Specifications for creep-resistant steels: Japan, in *Creep-Resistant Steels* (Woodhead Publishing, Sawston, Cambridge, England, 2008), pp. 155–173.
[3] J. R. Matthews and M. W. Finnis, J. Nucl. Mater. **159**, 257 (1988).
[4] S. K. Albert and S. Sundaresan, Using creep-resistant steels in nuclear reactors, in *Creep-Resistant Steels* (Woodhead Publishing, Sawston, Cambridge, England, 2008), pp. 597–636.
[5] O. D. Sherby and E. M. Taleff, Mater. Sci. Eng.: A **322**, 89 (2002).
[6] J. F. Nie and B. C. Muddle, Acta Mater. **48**, 1691 (2000).
[7] J. Dai, S. Zhu, M. A. Easton, W. Xu, G. Wu, and W. Ding, Mater. Charact. **88**, 7 (2014).
[8] M. Nastar and F. Soisson, 1.18 - Radiation-Induced Segregation A2 - Rudy J.M. Konings, in *Comprehensive Nuclear Materials* (Elsevier, Oxford, 2012), pp. 471–496.
[9] A. Barbu and A. J. Ardell, Scr. Metall. **9**, 1233 (1975).
[10] A. Barbu and G. Martin, Scr. Metall. **11**, 771 (1977).
[11] W. G. Wolfer, 1.01 - Fundamental Properties of Defects in Metals A2 - Rudy J.M. Konings, in *Comprehensive Nuclear Materials* (Elsevier, Oxford, 2012), pp. 1–45.
[12] J. P. Riviere, Radiation Induced Point Defects and Diffusion, in *Application of Particle and Laser Beams in Materials Technology* (Springer Netherlands, Dordrecht, 1995), pp. 53–76.
[13] T. Garnier, M. Nastar, P. Bellon, and D. R. Trinkle, Phys. Rev. B **88**, 134201 (2013).
[14] T. Garnier, V. R. Manga, D. R. Trinkle, M. Nastar, and P. Bellon, Phys. Rev. B **88**, 134108 (2013).
[15] P. H. Dederichs and K. Schroeder, Phys. Rev. B **17**, 2524 (1978).
[16] F. Larché and J. Cahn, Acta Metall. **33**, 331 (1985).
[17] A. R. Allnatt and A. B. Lidiard, *Atomic Transport in Solids* (Cambridge University Press, Cambridge, England, 1993).
[18] C. C. Battaile, *Recent Advances in Computational Study of Nanostructures*, Comput. Methods Appl. Mech. Eng. **197**, 3386 (2008).
[19] G. P. Purja Pun and Y. Mishin, Acta Mater. **57**, 5531 (2009).
[20] A. B. Sivak, V. M. Chernov, V. A. Romanov, and P. A. Sivak, *Proceedings of ICFRM-14*, J. Nucl. Mater. **417**, 1067 (2011).
[21] M. Nastar, V. Y. Dobretsov, and G. Martin, Philos. Mag. A **80**, 155 (2000).
[22] M. Nastar, Philos. Mag. **85**, 3767 (2005).
[23] D. R. Trinkle, arXiv:1608.01252.
[24] L.-Q. Chen, Annu. Rev. Mater. Res. **32**, 113 (2002).
[25] G. Boussinot, Y. Le Bouar, and A. Finel, Acta Mater. **58**, 4170 (2010).
[26] P.-A. Geslin, B. Appolaire, and A. Finel, Appl. Phys. Lett. **104**, 011903 (2014).
[27] J. H. Ke, A. Boyne, Y. Wang, and C. R. Kao, Acta Mater. **79**, 396 (2014).
[28] T. Garnier, V. R. Manga, P. Bellon, and D. R. Trinkle, Phys. Rev. B **90**, 024306 (2014).
[29] T. Garnier, Z. Li, M. Nastar, P. Bellon, and D. R. Trinkle, Phys. Rev. B **90**, 184301 (2014).
[30] G. S. Was, Point Defect Formation and Diffusion, in *Fundamentals of Radiation Materials Science: Metals and Alloys* (Springer Berlin Heidelberg, Berlin, Heidelberg, 2007), pp. 155–190.
[31] D. J. Hepburn, E. MacLeod, and G. J. Ackland, Phys. Rev. B **92**, 014110 (2015).
[32] J. D. Tucker, R. Najafabadi, T. R. Allen, and D. Morgan, J. Nucl. Mater. **405**, 216 (2010).
[33] E. Clouet and M. Nastar, Phys. Rev. B **75**, 132102 (2007).

[34] M. F. Sykes and D. S. Gaunt, J. Math. Phys. **14**, 1060 (1973).
[35] J. E. Westmoreland, J. A. Sprague, F. A. Smidt, and P. R. Malmberg, Radiat. Eff. **26**, 1 (1975).
[36] J. J. Carter, W. H. Howland, and R. W. Smith, Metall. Mater. Trans. A **46**, 93 (2015).
[37] A. V. Kozlov, V. L. Panchenko, K. A. Kozlov, I. M. Russkikh, and A. V. Kozlov, Phys. Met. Metallogr. **115**, 39 (2014).
[38] J. E. Guyer, D. Wheeler, and J. A. Warren, Comp. Sci. Eng. **11**, 6 (2009).